

Smart Scattering Scanning Near-Field Optical Microscopy

Simon Labouesse, Samuel C. Johnson, Hans A. Bechtel, Markus B. Raschke, and Rafael Piestun*

Cite This: *ACS Photonics* 2020, 7, 3346–3352

Read Online

ACCESS |



Metrics & More



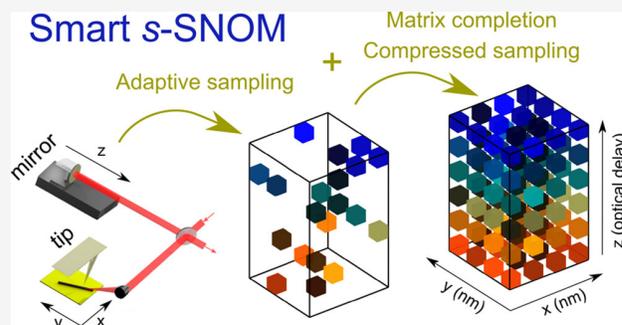
Article Recommendations



Supporting Information

ABSTRACT: Scattering scanning near-field optical microscopy (*s*-SNOM) provides spectroscopic imaging from molecular to quantum materials with few nanometer deep subdiffraction limited spatial resolution. However, in its conventional implementation *s*-SNOM is slow to effectively acquire a series of spatio-spectral images, especially with large fields of view. This problem is further exacerbated for weak resonance contrast or when using light sources with limited spectral irradiance. Indeed, the generally limited signal-to-noise ratio prevents sampling a weak signal at the Nyquist sampling rate. Here, we demonstrate how acquisition time and sampling rate can be significantly reduced by using compressed sampling, matrix completion, and adaptive random sampling, while maintaining or even enhancing the physical or chemical image content. We use fully sampled real data sets of molecular, biological, and quantum materials as ground-truth physical data and show how deep under-sampling with a corresponding reduction of acquisition time by 1 order of magnitude or more retains the core *s*-SNOM image information. We demonstrate that a sampling rate of up to 6× smaller than the Nyquist criterion can be applied, which would provide a 30-fold reduction in the data required under typical experimental conditions. Our smart *s*-SNOM approach is generally applicable and provides systematic full spatio-spectral *s*-SNOM imaging with a large field of view at high spectral resolution and reduced acquisition time.

KEYWORDS: *s*-SNOM, compressed sensing, matrix completion, adaptive sampling, denoising, near field



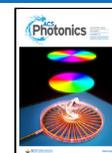
Infrared vibrational scattering scanning near-field optical microscopy (IR *s*-SNOM) provides nanoimaging with intrinsic vibrational, phonon, and electronic resonance contrast with chemical and material specificity at deep-subdiffraction spatial resolution (≤ 20 nm).^{1–5} Recent advances in IR *s*-SNOM enable nanoscopic chemical imaging of diverse materials, ranging from biological to molecular and quantum systems. The meso- and macroscopic behavior of these systems is determined by interactions at the nanoscopic level and therefore require imaging techniques with high spatial resolution and large fields of view. Typical data sets for IR *s*-SNOM chemical imaging include two spatial dimensions across the sample surface and one spectral dimension, for example, as obtained by scanning the reference arm mirror position in nano Fourier-transform infrared spectroscopy (nano-FTIR), see Figure 1A. Broadband IR light sources are desired for measuring multiple vibrational modes but are often limited by their low brilliance, which reduces the signal-to-noise ratio (SNR). Laser-based IR spectroscopy has high brilliance but is challenged by sample exposure when low repetition rate and high pulse energy lasers are used. Therefore, chemical nanoimaging of biological, molecular, and quantum systems with large spatial and spectral resolution over large fields of view has remained challenging because of the associated large multidimensional data sets whose

achievable SNR limits the acquisition rate. Modifications of *s*-SNOM to increase acquisition speed have been proposed^{6,7} but have not yet taken advantage of the large redundancy in *s*-SNOM data sets. Previous work showed that compressed sampling can reduce nano-FTIR acquisition time using spectral sparsity.⁸ Further, compressed sensing has been adapted⁹ for spatio-spectral nano-FTIR imaging and augmented by spatial regularization. While compressed sampling and matrix completion have been used intensively for hyperspectral imaging,^{10–12} their full potential has not yet been exploited for *s*-SNOM. Matrix completion^{13,14} relies on the hypothesis that only a small number of chemical species, compositional characteristics, or structural features are present in the sample, which is in fact typically the case for most samples imaged with *s*-SNOM.

In this work we address this problem of reducing the amount of acquired data while maintaining physical relevance by using prior knowledge and an adaptive sampling algorithm tailored

Received: April 6, 2020

Published: November 12, 2020



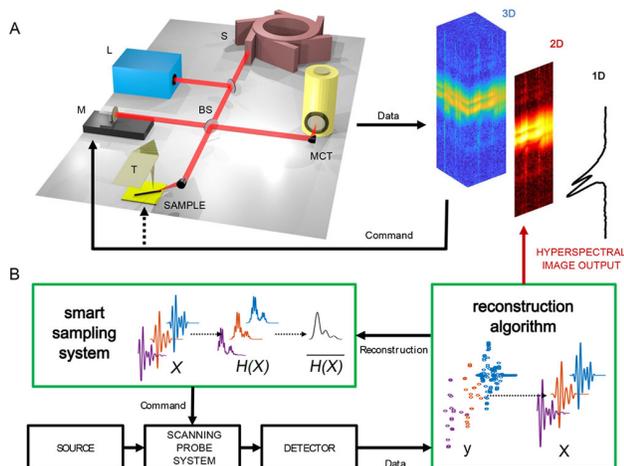


Figure 1. Smart *s*-SNOM schematic: (A) Light source laser L or synchrotron S, beam splitter BS, scanning mirror M on reference arm. Sample on scanning stage under the tip T, point detector mercury–cadmium–telluride on MCT. Hyperspectral images can be acquired by scanning the mirror and the sample. In the case of a 2D grid scan, or of a 1D line scan of the sample, the final output is, respectively, a 3D or 2D hyperspectral image. If the sample is not moved, but only the mirror is scanned, the final output is a 1D spectrum. (B) Diagram of smart *s*-SNOM. Our contribution: smart sampling system, provides a list of positions of the scanning mirrors for each sample point and reconstruction algorithm, to estimate the value of the missing data and, hence, recreates a fully sampled hyperspectral image X . At each new spatial position of the sample, an intermediate reconstruction is calculated in order to evaluate an averaged envelope $\overline{H}(X)$ of the interferograms. $\overline{H}(X)$ is normalized and used as a random distribution to select the mirror positions for the next sample position.

for *s*-SNOM. First, we demonstrate a reduction in data acquisition by using a combination of prior physical knowledge about the light source, the spectral sparsity, and a limited number of distinct chemical species. The analysis of the impact of each hypothesis individually, and their interplay, leads to the design of an effective reconstruction algorithm for full spatio-spectral *s*-SNOM imaging from compressed measurements. We show that a compression of up to 96.6% (1/30 sample) compared to acquisition under conventional uncompressed conditions can be achieved without sacrificing physically meaningful information in the nano-FTIR images or spectra. Further, we develop an adaptive algorithm for positioning the reference arm mirror at each spatial position of the sample. We note that random sampling is a universal strategy adapted for compressed sampling and matrix completion.^{15,16} We propose to estimate the normalized average envelope of the local interferograms to use as a probability distribution to select the random mirror positions. This approach acquires data in the most relevant parts of the interferogram with high probability, see Figure 1B. To study the achievable performance of this new approach of smart *s*-SNOM, we use fully sampled real data sets of biological, quantum, and molecular materials¹⁷ as ground truth. A subsampled measurement is extracted from the ground truth measurement using smart sampling, then a reconstruction algorithm recovers the remaining not-sampled data by using prior knowledge about the light source and the sample.

METHODS

Compressed sampling (CS) and matrix completion (MC) are well suited for *s*-SNOM to reduce the number of measurements needed to have a large field of view at high spectral resolution. In the following subsections, we motivate choices to create reconstruction algorithms based on CS and MC and describe an adaptive scan strategy for the reference arm mirror position. Conventionally, the sample is raster scanned under an atomic force microscope (AFM) tip to image a rectangular area of the sample; the spatial points are distributed along a regular discrete grid of evenly spaced points. At a given spatial position of the tip, the reference arm mirror is scanned to acquire an interferogram. One data point of the interferogram corresponds to one mirror position, which corresponds to one optical delay between reference and signal arms. In practice, the mirror is translated with a constant speed and measurements are periodically performed to get regularly spaced delays.¹⁸ Here we propose to use only a small fraction of the mirror positions that are standard in conventional *s*-SNOM acquisition. In order to recover the missing data points, we exploit prior knowledge of the sample and the light source. See Supporting Information, “Experiment acquisition details”.

Compressed Sampling (CS). Infrared spectroscopy resolves spectral peaks from, for example, molecular vibrations, which are specific to the molecular identity and their local chemical environment. Each spatial point of an *s*-SNOM measurement contains a mixture of distinct chemical species that, when spectroscopically measured, yield a combination of vibrational spectra of multiple local chemical species. *s*-SNOM spectra are usually composed of a few resonance peaks and are, thus, in principle, sparse signals.

Unfortunately, the sparsity assumption is not always correct; for instance, the free carrier response can contribute to a wide spectral range. In those cases, only other prior knowledge, as described in the following sections, can be used. The number of mirror positions in FTIR spectroscopy can be reduced using concepts of compressed sampling.^{8,9} Compressed sampling^{19–21} is a well-established technique to efficiently acquire and reconstruct a signal. Two main assumptions are required, sparsity (here of the spectrum) and mathematical incoherence of the sensing matrix.¹⁹ In our context, incoherence means that every point of an interferogram is a different linear combination of each frequency point of the corresponding spectrum. Here, the interferogram and the spectrum are linked by a Fourier transform. It is well-known in signal processing that the Fourier transform associated with a random selection of samples leads to an incoherent sensing matrix.²² Therefore, in *s*-SNOM, all the conditions are met to use CS on the spectral dimension. Moreover, spectral peaks can only be detected if they are within the light source bandwidth. Hence, the spectrum is reconstructed only inside the light source bandwidth and set to zero outside. When the light source is a laser, this can be used to greatly reduce the number of necessary samples acquired.⁶ The spectral portion outside the light source bandwidth does not affect the measurement and is considered to be composed of zeros. A truncated Fourier transform on the accessible part of the spectrum is used to reduce the problem dimension and to increase computation speed and compression factor.

Matrix Completion (MC). *s*-SNOM spectra are combinations of a few distinct chemical vibrational spectra. Under mild assumptions, this leads to a small rank measurement matrix

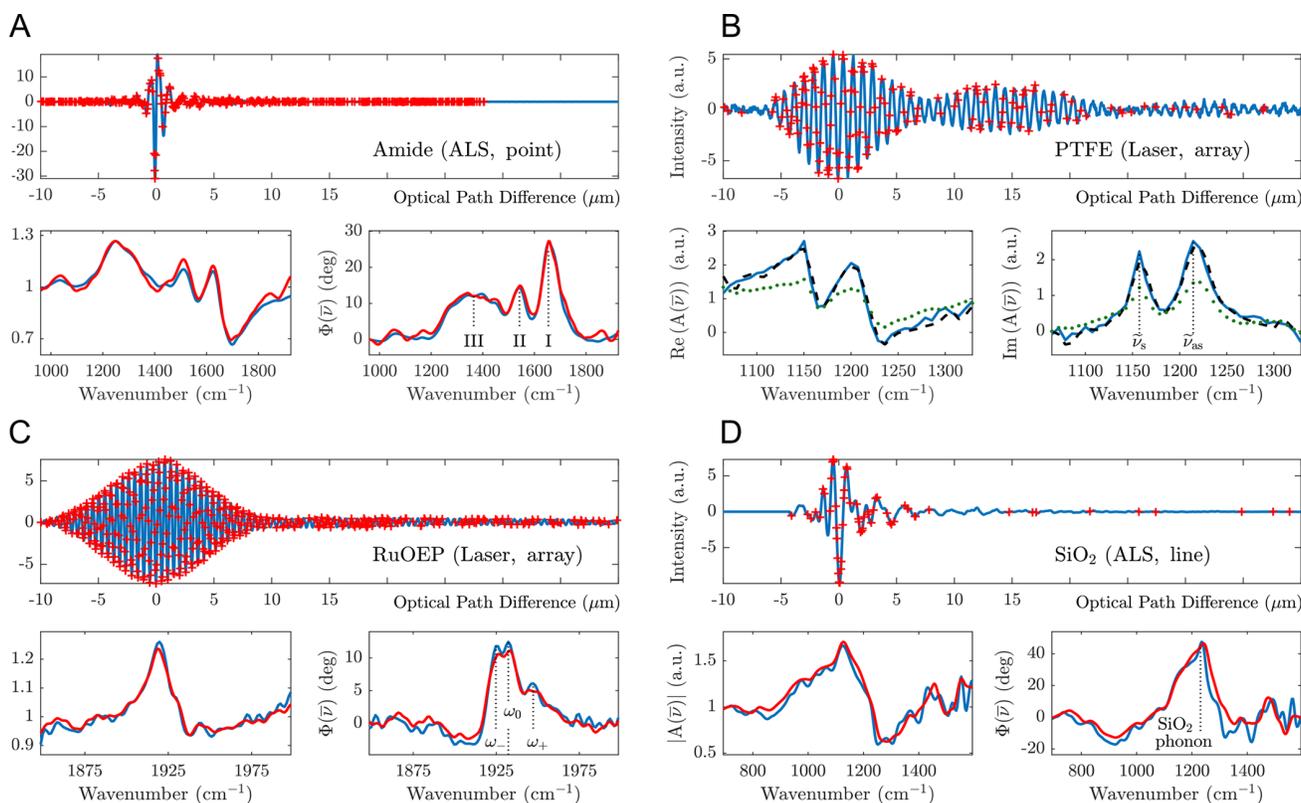


Figure 2. Application of smart *s*-SNOM to different materials systems (biological, molecular, and quantum), different light sources (Laser, ALS synchrotron), and different spatial scanning (single point, line, and 2D scan). Fully sampled data sets acquired experimentally (blue curves). Mirror positions selected by our adaptive sampling strategy (red crosses). Reconstructed spectrum in amplitude/phase or $|A(\bar{z})|/\Phi(\bar{z})$ and real/imaginary part or $\text{Re}(A(\bar{z}))/\text{Im}(A(\bar{z}))$ (red and black dotted curves, respectively). For the PTFE sample, reconstruction from uniformly sampled measurements without the use of adaptive sampling (green dotted curves). The reduction factor (*R*) is, respectively, 17, 30, 4, and 30. The compression factor (*CF*) is, respectively, 1, 4, 1.6, and 6.5. The regularization parameter called *Nuc* is, respectively, 0, 5, 0.75, and 0.005. The regularization parameter l_1 is, respectively, 0, 10^{-6} , 0.01, 4×10^{-5} (see Supporting Information, “Algorithm”).

when the number of chemical species in the sample is small compared to the number of spatial measurement points. Under a linear mixing assumption it can be shown that the rank of the measurement matrix will be smaller than the number of chemical species in the sample^{23,24} (see Supporting Information, “Low rank assumption”). Matrix completion is used to complete matrices with missing entries under the approximate low rank assumption.^{13,14} Regular *s*-SNOM data can be rearranged in a matrix form with interferograms in rows, where each row corresponds to a given spatial position of the tip. When only a few random positions of the mirror are selected, the missing data in the matrix is suitable for recovery as missing entries because the matrix is low rank. MC is not sensitive to the complex spatial distribution of the chemical species; therefore, it remains a useful tool, even for samples with random uncorrelated spatial distributions of the chemical species.

Adaptive Random Sampling. Redundancies in *s*-SNOM data can be exploited to recover a full field of view and a complete spectral image from fewer measurements. In addition, we propose an adaptive selection of the most appropriate sampling positions for the reference arm mirror at the next tip position. Intuitively, the sampling should select parts of the interferogram that convey the most variations. Thus, we propose tuning the probability distribution of the random sample selection as close as possible to the envelope of the interferograms. *s*-SNOM samples can show a wide diversity

of interferogram envelopes, which emphasizes the necessity for an adaptive strategy to select the best mirror positions to acquire data. At the beginning of an acquisition, the only prior knowledge available is the spectral bandwidth of the light source and the sparsity of the spectrum. Therefore, for the first sample spatial position, we use a uniform random distribution to select the reference arm mirror positions where data will be collected. The number of samples to be acquired can be determined by using the Nyquist criterion and the sparsity assumption. For the following spatial position, we have more information from the previous measurement. Hence, we propose tuning the random distribution used to select the mirror positions so that it is as close as possible to the envelope of the interferogram. We reconstruct all of the interferograms at previous spatial positions and calculate their envelopes. We use the average of these envelopes to generate the probability distribution for spectral sampling at the next sample position. The sampling rate is continually reduced throughout the measurement such that the desired final compression factor is achieved (more details can be found in Supporting Information, “Parameter tuning”). Similar to MC, the performance gain due to our adaptive sampling strategy is sensitive to the number of pure chemical species in the sample as well as to the number of appearances of each chemical species. However, the performance gain does not depend on the spatial distribution of the chemical species.

Experimentally, smart *s*-SNOM moves the scanning mirror (see Figure 1) to only some specific positions dictated by the adaptive sampling strategy. This kind of experiment is emulated by using the adaptive sampling selection rules on the data provided by a conventional *s*-SNOM experiment. The fully sampled data set can then be used both as a ground truth to calculate errors, like relative mean square error, or to compare the peak positions of the reconstruction. In our algorithm, we made the choice to minimize a criterion enforcing fidelity to data using a quadratic norm with penalization added to enforce the sparsity of the spectrum and the low rank assumption. The criterion is convex and has two parameters λ_1 and λ_* to tune how sparse and how low rank the reconstruction should be, respectively. We then use a generalized forward-backward algorithm²⁵ to minimize this criterion. A detailed description of the criterion and of the algorithm is presented in the Supporting Information, "Algorithm". In the following we demonstrate how our strategy performs on different samples and how well physically relevant information is kept in the reconstructions.

RESULTS

s-SNOM imaging can be used on a broad class of samples (see Figure 2), including biological, molecular, and quantum materials. We tested our algorithms with a representative member of each of these material types and with two different light sources, including a laser and a synchrotron (Advanced Light Source ALS). Light source properties affect the interferogram shape (see Figure 2). Specifically, the synchrotron's broad bandwidth leads to a sparser representation than that of a laser. We quantify the compression with two different metrics. The ratio between the number of acquired samples for a fully sampled acquisition and for a smart *s*-SNOM acquisition is called the reduction factor (*R*). The experimental data used as ground truth in this paper are oversampled to ensure Nyquist sampling above the highest frequency of the light source. Furthermore, the mirror displacement range is scanned to achieve a fixed spectral instrument resolution that is narrower than the observed spectral features. Therefore, we also give the ratio between minimally sampled acquisitions (at Nyquist rate and smallest mirror motion range) and smart *s*-SNOM sampling, which is called the compression factor (CF). We emphasize that, at the experimental integration time per sample, Nyquist sampling would greatly reduce the quality of the spectrum; therefore, we use *R* as a fair ratio to be highlighted. Laser-based broadband measurements (nano-FTIR) and synchrotron IR nanospectroscopy (SINS) were performed as previously described in ref 17 (see also Supporting Information). We considered a range of sample types and light sources for a robust interpretation of smart *s*-SNOM reconstructions.

The first data set shown in Figure 2A is a synchrotron radiation based measurement of 400 nm thick γ -globulin referenced to Si, as described in ref 17. This measurement highlights the difficulty of measuring multiple chemical resonances with a low brilliance light source. The spectrum of gamma-globulin shows the characteristic amide resonances (I, II, and III) of a protein and are indicated in Figure 2A. Only one spatial point is acquired; therefore, only sparsity of the spectrum and light source bandwidth priors can be used in this case. For this particular sample the sparsity of the spectrum in the light source bandwidth does not enable a compression

factor over 1. Here, only the bandwidth prior has an effect on the compression. However, the reduction factor *R* is 17.

The second data set shown in Figure 2B corresponds to a laser based measurement of oriented PTFE referenced to gold. We examine the real and imaginary part of nano-FTIR spectra from PTFE, rather than the amplitude and phase, as the oscillator strength is too strong for the typical approximation between phase and imaginary spectra. The achieved compression factor is 4, well below the minimum number of the necessary points without the sparsity and small rank assumptions. Therefore, MC and/or CS are useful to improve the CF for PTFE samples. The separate effect of CS and MC is demonstrated in Figure 3 using the PTFE data set. The influence of *R* on the characterization of the two PTFE peaks is illustrated in Figure 4.

The third data set is a laser based measurement in a molecular electronic material of a metal carbonyl vibration (2,3,7,8,12,13,17,18-octaethyl-21H,23H-porphine ruthenium(II) carbonyl). This example demonstrates the difficulty of accurately determining multiple spectral features of varying

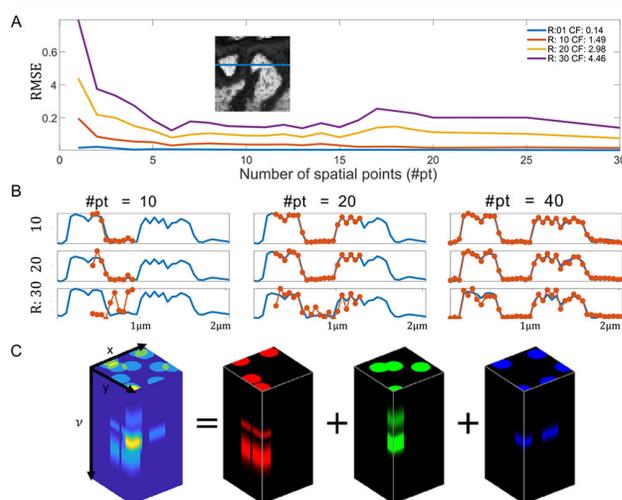


Figure 3. Illustration of the effect of low rank assumption on the reconstruction error. We use a PTFE hyperspectral array scan to emulate an acquisition of different sized line scans. The position of the spatial line scanned is indicated with a blue line on the image of panel B). (A) Plots of relative mean square error as a function of the number of spatial points for different reduction factors. The largest quality improvement occurs between 1 and 6 spatial points, this is an indication of the MC influence on the reconstruction quality. This can be different for other samples with a higher diversity of chemical species. (B) For each number of points used (10, 20, and 40 pixels), different reduction factors are emulated: 10, 20, and 30 by reducing more and more the number of positions used for the mirror. The spatial evolution of the spectrum amplitude at $\tilde{\nu}_{as}$ for ground truth is plotted in blue and the reconstructions in red. At a given reduction factor the visual quality of the reconstruction improves with the number of spatial points sampled, this is also an indication of the MC influence. (C) Illustration of the principle of matrix completion. Each color red, green, and blue corresponds to one chemical species with a specific spectrum. Those images are separable in space (x, y) and frequency (ν) and are, therefore, considered rank one images. In the case of a linear mixing model, the final hyperspectral image is a sum of a few (rank one) of these images if the number of chemical species is small in the sample. This explains the link between small rank assumption on hyperspectral images and the number of chemical species.

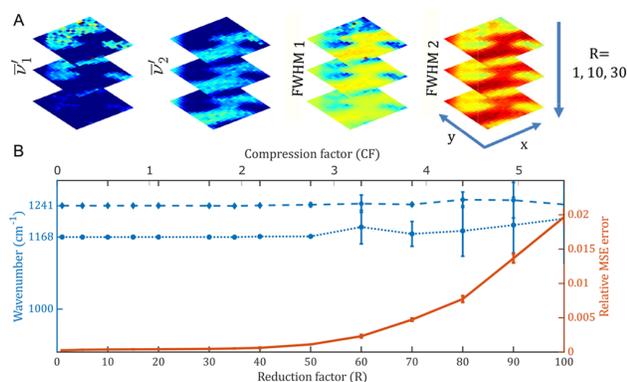


Figure 4. Extraction of physically relevant information from resonance peaks at different reduction factors. (A) Characterization of the two spectral peaks of the PTFE sample located at $\nu_1 = 1168 \text{ cm}^{-1}$ and $\nu_2 = 1241 \text{ cm}^{-1}$. Each stack corresponds to three images obtained from reconstruction at different reduction factors (from top to bottom, respectively, 1, 10, and 30). Each peak is characterized by its estimated position ν' and full width at half-maximum FWHM. (B) Plot of the relative mean square error between reconstruction and ground truth in red. Plot of the localization of the two peaks in blue as a function of the compression factor (top axis) and to the reduction factor (bottom axis). The standard deviation of the peak localization increases with compression factor, leading to potential physical misinterpretation of the reconstruction for high reduction or compression factors.

resonant strengths. The center resonance ω_0 splits into ω_- and ω_+ , see Figure 2C, as the crystallinity of the nanocrystals are increased. These resonances are close to each other and are of similar strength, hence, increasing the difficulty of reducing the number of measurements. Nonetheless, we achieve a reduction factor R of 4. It is worth noting that the ground truth spatial sampling was irregular, namely, only a subset of a regular rectangular grid positions were used. Our algorithm does not use the relative position of the spatial point, therefore any spatial scanning pattern is compatible with smart s -SNOM.

The fourth data set is a FIR measurement of the silicon dioxide (SiO_2) phonon performed with synchrotron radiation. The ground truth corresponds to a line scan of the SiO_2 sample. A reduction factor of 30 was achieved on this sample corresponding to a CF of 6.5. Therefore, having an adaptive sampling strategy is attractive to collect data only at relevant mirror positions, as shown in Figure 2D. AFM images of the four data sets are shown in Figure S1, as well as the spatial position of the tip, where s -SNOM interferograms were acquired.

Adaptive Sampling Influence. The impact of the adaptive sampling influence can be seen by comparing the reconstructed spectrum from data selected with a uniform random position for the reference mirror to the reconstructed spectrum achieved from data selected with our adaptive sampling strategy (see, respectively, green and black dotted curves in Figure 2B). We see that adaptive sampling dramatically improves the reconstruction quality. Figure 2 displays a broad range of interferogram shapes. In each case, our adaptive strategy evaluates the average envelope and therefore allows us to select mirror positions in the most relevant parts of the interferograms. We see the selected mirror positions plotted with red crosses in Figure 2D, showing that most of the sampled positions are near the zero-path difference (ZPD) region of the interferogram due to the distribution. In

this case, improved spectral resolution achieved by larger mirror displacements does not appear to contribute new information; thus, points closer to the ZPD region are sufficient to reproduce the spectrum. In Figure 2A, the mirror positions are drawn from a uniform distribution because only one spatial point is used; therefore, the acquisition has to be performed without any prior knowledge of the interferogram shape.

Compressed Sampling Influence. In Figure 2, the γ -globulin sample is probed at only one spatial position. Therefore, only spectral compressed sampling could be used to reduce the number of measurements. Unfortunately the resulting spectrum is not sparse compared to the bandwidth of the synchrotron. We observe that the compression factor is one, but nonetheless, the reduction factor is 17. The knowledge of the bandwidth allows, in this case, to work with $17\times$ less data. Figure 3A shows, for the PTFE sample, the relative mean square error (RMSE) between reconstruction and ground truth for four different compression factors (1, 10, 20, and 30). The RMSE for only one spatial point are 0.019, 0.197, 0.440, and 0.794, respectively. These errors are obtained using optimal parameter settings 0, 0.1, 0.1, 0.1 for the l_1 parameter and 0, 0, 0, and 0 for the nuclear parameter, respectively (see Supporting Information, “Algorithm”). We notice that the nuclear parameter is always 0, indicating the fact that MC is not useful when only one spatial point is probed. For comparison, we perform a reconstruction with the l_1 parameter also set to 0 to see the effect of the l_1 norm on the reconstruction of the resulting RMSE of 0.0185, 1.42, 1.53, and 1.6, respectively. We notice that the RMSE for compression factors of 10, 20, and 30 is greatly reduced using the l_1 norm (by 70% in average). As a result, we conclude that compressed sensing improves the performance for the PTFE sample, in agreement with similar effects observed in refs 8 and 9.

Matrix Completion Influence. The effect of matrix completion depends on the number of spatial points acquired. If there are fewer spatial points than the number of pure chemical mixtures in the sample, matrix completion becomes irrelevant. To show how MC is used in our reconstruction, we study the effect of the number of spatial points on the quality of the reconstruction of the PTFE sample. The experiment consists of emulating line scan experiments of different sizes and different compression ratios. The curves displayed in Figure 3A show that the relative mean square error (RMSE) of the reconstruction compared to the ground truth, decrease with the number of spatial points sampled. Moreover, we see that MC enables a higher CF compared to CS alone. In Figure 3B, the reconstruction of a 1D spatial section is shown for different number of spatial points and different reduction factor. There is a clear relation between R , the number of spatial points and the quality of the reconstruction. This shows the effectiveness of MC on the PTFE sample. We also observe that only a limited number of spatial points is needed to fully use MC (around six spatial points for PTFE). This is an indication that the number of chemical species is indeed small in this sample (see Figure 3C).

Physical Relevance of Reconstructions. In some applications users are only interested in the characteristics of the spectral peaks. In the PTFE example, there are two peaks, corresponding to the symmetric and antisymmetric modes that convey the physically relevant information. They are characterized by their location at $\tilde{\nu}_1 = 1168 \text{ cm}^{-1}$ and $\tilde{\nu}_2 = 1241 \text{ cm}^{-1}$, full width at half-maximum, amplitude, and phase.

Figure 4A illustrates the capacity to extract this information from smart *s*-SNOM data at different reduction factors. Color bars of each image correspond to an estimate of one of these parameters, each pixel corresponds to a spatial position of the sample. Ground truth value of the parameters are shown in the top images of each stack, where $R = 1$, and are compared with the $R = 10$ and 30 cases. In Figure 4B, an estimation of the peaks positions appears to be unbiased for a reduction factor up to 100; however, the standard deviation increases with reduction factor (see error bars of blue curves). A good estimation of the peak's position, width, and relative amplitude can be achieved for R up to 30. We also observe a denoising effect of our algorithm, where the sparsity assumption and the low rank assumption used in our algorithm allow us to reject a significant part of the noise contained in the reconstruction. This is explained by the fact that the noise component of the data is not sparse in the Fourier domain and is not low rank.

DISCUSSION

While signal processing for hyper-spectral imaging is a broad field, we presented a focused development of choices to create a smart *s*-SNOM approach taking into account its physical properties. In this section, we discuss the particular choices made and avoided as well as the limitations of the technique.

CS for Spatial Dimension. Similar to the temporal or spectral dimension, spatial dimensions carry redundancies because samples are composed of finite types of molecules that are typically clustered or arranged in domains. The wavelet transform of such samples is known to be sparse.²⁶ Additionally, the 2D curvelet transform has been proven to be sparse for images that are piece-wise smooth with smooth boundaries.²⁷ This could be used to reduce the number of spatial positions of the tip using CS. As an example, CS has been used in AFM to increase acquisition speed.²⁸ CS along the spatial dimensions can be combined with CS in the spectral dimension and would fall in a family called Kronecker CS.²⁹ In the case of a sample containing a spatially isolated chemical species, the Wavelet domain would no longer yield a sparse image and therefore would not comply with CS requirements. It is arguable whether this would be an interesting feature to be determined and hence whether the wavelet domain sparsity should be used or not. Moreover, as a practical note, performing this additional step slows down the reconstruction because at each iteration one needs to perform a spatial wavelet transform for each mirror position used. Given the small compression potential, the strong hypothesis on the sample and the added algorithmic cost, we decided not to implement this approach at this time.

Scanning. We note that mirror scanning stages have limitations not included in our model. Indeed, speed and precision of the mirror and tip motion are linked to the trajectory used. Lissajous curves are a good candidate for scanning strategy.¹² Our adaptive selection of the mirror positions would need to be modified to take these limitations into account. Moreover, a multipass strategy could be used to improve the selection of the mirror position. Nonetheless, our contribution clearly demonstrates the potential of using an adaptive strategy to reduce *s*-SNOM acquisition time. Introducing scanning limitations in our model could lead to faster implementation of smart *s*-SNOM.

Algorithm. If the rank was known in advance, Non-Negative Matrix Factorization (NMF)³⁰ could be applied. One can argue that an upper bound of the rank can be derived.

Another disadvantage of NMF is that the problem becomes non convex, therefore we decided not to use NMF. Alternatively, we chose to minimize a convex criterion with a generalized forward–backward algorithm for its simplicity, its speed, and its flexibility to add and try multiple penalization terms. We chose to use l_1 norm and $l_{2,*}$ nuclear norm to enforce the sparsity of the reconstructed spectra and to reduce the rank of the reconstruction, respectively. Notwithstanding, one could think about many other penalization functions. For instance, we tried an $l_{1,2}$ penalization, but the effect on the reconstruction quality is smaller than the two penalization functions we use. Adding a penalization function also increases the number of parameters to tune; therefore, we tried to minimize the number of penalization functions. We still have two parameters to tune in our criterion, see Supporting Information, “Parameters tuning” for more information. An automatic tuning strategy like cross validation^{31,32} could be tested.

A key aspect of smart *s*-SNOM is that it decreases acquisition time without sacrificing meaningful information. This might seem counterintuitive because of the potential impact on SNR of the reduction in total integration time. However, the lost integration time from missing data points is offset by both the reconstruction and the denoising effects. In fact, while conventional sampling is inefficient with the data collection, as prior knowledge is not used to inform sampling, smart *s*-SNOM reconstruction makes use of the prior knowledge of the object observed to reject noise and to recover missing acquisitions information.

PERSPECTIVE AND SUMMARY

We propose a strategy to compress *s*-SNOM measurements and therefore greatly reduce acquisition time. To achieve that, we reduce the number of mirror positions needed at each location of the sample by exploiting redundancies in the *s*-SNOM data set. Known prior knowledge, like bandwidth of the light source, spectral sparsity, and the limited number of distinct chemical species, is used to reduce the necessary measurements. By using the same prior knowledge in our adaptive selection of the sampled mirror positions, we greatly improve the performance of *s*-SNOM. Smart *s*-SNOM opens the way to applications where a wide field of view and a good spectral resolution are both required apart from the nanometric resolution.

ASSOCIATED CONTENT

Supporting Information

The Supporting Information is available free of charge at <https://pubs.acs.org/doi/10.1021/acsp Photonics.0c00553>.

Experimental and analytical details (PDF)

AUTHOR INFORMATION

Corresponding Author

Rafał Piestun – Department of Electrical, Computer, and Energy Engineering, University of Colorado, Boulder, Colorado 80309, United States; orcid.org/0000-0002-1240-7049; Email: piestun@colorado.edu

Authors

Simon Labouesse – Department of Electrical, Computer, and Energy Engineering, University of Colorado, Boulder, Colorado 80309, United States

Samuel C. Johnson – Department of Physics, Department of Chemistry, and JILA, University of Colorado, Boulder, Colorado 80309, United States; orcid.org/0000-0003-0567-5026

Hans A. Bechtel – Advanced Light Source Division, Lawrence Berkeley National Laboratory, Berkeley, California 94720, United States

Markus B. Raschke – Department of Physics, Department of Chemistry, and JILA, University of Colorado, Boulder, Colorado 80309, United States; orcid.org/0000-0003-2822-851X

Complete contact information is available at:

<https://pubs.acs.org/10.1021/acsp Photonics.0c00553>

Author Contributions

S.L., S.C.J., H.A.B., M.B.R., and R.P. designed the research; S.L. and S.C.J. performed the research; S.L., S.C.J., H.A.B., M.B.R., and R.P. analyzed the data; S.L. wrote the paper with contributions from S.C.J., H.A.B., M.B.R., and R.P.; M.B.R. and R.P. conceived and supervised the project.

Notes

The authors declare the following competing financial interest(s): The authors submitted a patent application through the University of Colorado.

ACKNOWLEDGMENTS

We acknowledge funding from the NSF Science and Technology Center on Real-Time Functional Imaging (STROBE) under DMR1548924. This research used resources of the Advanced Light Source, a DOE Office of Science User Facility under Contract No. DE-AC02-05CH11231.

REFERENCES

- (1) Berweger, S.; Nguyen, D. M.; Muller, E. A.; Bechtel, H. A.; Perkins, T. T.; Raschke, M. B. Nano-chemical infrared imaging of membrane proteins in lipid bilayers. *J. Am. Chem. Soc.* **2013**, *135* (49), 18292–18295.
- (2) Zenhausern, F. Y. H. K.; Martin, Y.; Wickramasinghe, H. K. Scanning interferometric apertureless microscopy: optical imaging at 10 angstrom resolution. *Science* **1995**, *269* (5227), 1083–1085.
- (3) Inouye, Y.; Kawata, S. Near-field scanning optical microscope with a metallic probe tip. *Opt. Lett.* **1994**, *19* (3), 159–161.
- (4) Bachelot, R.; Gleyzes, P.; Boccaro, A. C. Near-field optical microscope based on local perturbation of a diffraction spot. *Opt. Lett.* **1995**, *20* (18), 1924–1926.
- (5) Keilmann, F.; Hillenbrand, R. Near-field microscopy by elastic light scattering from a tip. *Philos. Trans. R. Soc., A* **2004**, *362* (1817), 787–805.
- (6) Johnson, S. C.; Muller, E. A.; Khatib, O.; Bonnin, E. A.; Gagnon, A. C.; Raschke, M. B. Infrared nanospectroscopic imaging in the rotating frame. *Optica* **2019**, *6* (4), 424–429.
- (7) Schnell, M.; Carney, P. S.; Hillenbrand, R. Synthetic optical holography for rapid nanoimaging. *Nat. Commun.* **2014**, *5*, 3499.
- (8) Katz, O.; Levitt, J. M.; Silberberg, Y. Compressive fourier transform spectroscopy. In *Frontiers in Optics 2010/Laser Science XXVI*; Optical Society of America, 2010; p FTuE3.
- (9) Kästner, B.; Schmähling, F.; Hornemann, A.; Ulrich, G.; Hoehl, A.; Kruskopf, M.; Pierz, K.; Raschke, M. B.; Wübbeler, G.; Elster, C. Compressed sensing for nano-spectroscopy and nano-imaging. *Opt. Express* **2018**, *26* (14), 18115–18124.
- (10) Golbabaee, M.; Vanderghyest, P. Hyperspectral image compressed sensing via low-rank and joint-sparse matrix recovery. In *Acoustics, Speech and Signal Processing (ICASSP), 2012 IEEE International Conference on* **2012**, *IEEE*, 2741–2744.

(11) Soldevila, F.; Dong, J.; Tajahuerce, E.; Gigan, S.; de Aguiar, H. B. Fast compressive raman bio-imaging via matrix completion. *Optica* **2019**, *6* (3), 341–346.

(12) Lin, H.; Liao, C.-S.; Wang, P.; Kong, N.; Cheng, J.-X. Spectroscopic stimulated raman scattering imaging of highly dynamic specimens through matrix completion. *Light: Sci. Appl.* **2018**, *7* (5), 17179.

(13) Candès, E. J.; Recht, B. Exact matrix completion via convex optimization. *Foundations of Computational mathematics* **2009**, *9* (6), 717.

(14) Candès, E. J.; Plan, Y. Matrix completion with noise. *Proc. IEEE* **2010**, *98* (6), 925–936.

(15) Candès, E. J.; Tao, T. Near-optimal signal recovery from random projections: Universal encoding strategies? *IEEE Trans. Inf. Theory* **2006**, *52* (12), 5406–5425.

(16) Candès, E. J.; Tao, T. The power of convex relaxation: Near-optimal matrix completion. *IEEE Trans. Inf. Theory* **2010**, *56* (5), 2053–2080.

(17) Bechtel, H. A.; Muller, E. A.; Olmon, R. L.; Martin, M. C.; Raschke, M. B. Ultrabroadband infrared nanospectroscopic imaging. *Proc. Natl. Acad. Sci. U. S. A.* **2014**, *111* (20), 7191–7196.

(18) Snively, C. M.; Katzenberger, S.; Oskarsdottir, G.; Lauterbach, J. Fourier-transform infrared imaging using a rapid-scan spectrometer. *Opt. Lett.* **1999**, *24* (24), 1841–1843.

(19) Candès, E. J. Compressive sampling. *Proceedings of the international congress of mathematicians* **2007**, *3*, 1433–1452.

(20) Donoho, D. L. Compressed sensing. *IEEE Trans. Inf. Theory* **2006**, *52* (4), 1289–1306.

(21) Candès, E. J.; Wakin, M. B. An introduction to compressive sampling. *IEEE signal processing magazine* **2008**, *25* (2), 21–30.

(22) Candès, E. J.; Romberg, J.; Tao, T. Robust uncertainty principles: Exact signal reconstruction from highly incomplete frequency information. *IEEE Trans. Inf. Theory* **2006**, *52*, 489–509.

(23) Bioucas-Dias, J. M.; Plaza, A.; Dobigeon, N.; Parente, M.; Du, Q.; Gader, P.; Chanussot, J. Hyperspectral unmixing overview: Geometrical, statistical, and sparse regression-based approaches. *IEEE journal of selected topics in applied earth observations and remote sensing* **2012**, *5* (2), 354–379.

(24) Udell, M.; Townsend, A. Why are big data matrices approximately low rank? *SIAM Journal on Mathematics of Data Science* **2019**, *1* (1), 144–160.

(25) Raguet, H.; Fadili, J.; Peyré, G. A generalized forward-backward splitting. *SIAM Journal on Imaging Sciences* **2013**, *6* (3), 1199–1226.

(26) Antonini, M.; Barlaud, M.; Mathieu, P.; Daubechies, I. Image coding using wavelet transform. *IEEE Transactions on image processing* **1992**, *1* (2), 205–220.

(27) Candès, E. J.; Donoho, D. L. Curvelets: A surprisingly effective nonadaptive representation for objects with edges. *Technical Report*, Stanford Univ Dept of Statistics, 2000.

(28) Luo, Y.; Andersson, S. B. A continuous sampling pattern design algorithm for atomic force microscopy images. *Ultramicroscopy* **2019**, *196*, 167–179.

(29) Duarte, M. F.; Baraniuk, R. G. Kronecker compressive sensing. *IEEE Transactions on Image Processing* **2012**, *21* (2), 494–504.

(30) Lee, D. D.; Seung, H. S. Learning the parts of objects by non-negative matrix factorization. *Nature* **1999**, *401* (6755), 788.

(31) Geisser, S. *Predictive Inference*; Routledge, 2017.

(32) Fan, J.; Li, R. Variable selection via nonconcave penalized likelihood and its oracle properties. *J. Am. Stat. Assoc.* **2001**, *96* (456), 1348–1360.